ANNULAR SEALS OF HIGH ENERGY CENTRIFUGAL PUMPS: PRESENTATION OF FULL SCALE MEASUREMENT*

S. Florjancic and R. Stürchler
Sulzer Brothers, Limited
Winterthur, Switzerland

T. McCloskey
Electric Power Research Institute
Palo Alto, California, U.S.A.

Prediction of rotordynamic behaviour for high energy concentration centrifugal pumps is a challenging task which still imposes considerable difficulties. While the mechanical modelling of the rotor is solved most satisfactorily by FE techniques, accurate boundary conditions for arbitrary operating conditions are known for journal bearings only. Little information is available on the reactive forces of annular seals, such as neck ring and interstage seals and balance pistons, and on the impeller interaction forces.

The present work is focused to establish reliable boundary conditions at annular seals. For this purpose a full scale test machine was set up and smooth and serrated seal configurations measured. Dimensionless coefficients are presented and compared with a state of the art theory.

1. INTRODUCTION

Machine speed, head per stage, and power concentration of multi-stage centrifugal pumps have increased steadily during the last few decades. The increasing power concentration has often contributed to reliability problems, and often rotordynamic phenomena appear to be the main cause (ref. 1). Dynamic interaction forces between rotor and casing will always be present, and may even lead to destruction of the machine. Thus rotordynamic considerations become very important for high energy pumps; reliability of rotating equipment depends strongly on optimized rotordynamic behaviour.

With readily available computer codes (ref. 2), the rotor system can be modelled very well and optimization is possible in the design stage, provided the boundary conditions are known accurately enough. Costly changes after field tests, or more likely after break downs, will be less than optimum and can be avoided.

*This work at Sulzer Brothers was supported partially by EPRI under contract RP 1884-10.

Besides well known rotor casing interaction within journal bearings (refs. 3, 4, 5) and reaction forces at the impeller itself (refs. 6, 7), boundary conditions for annular seals are of main interest. Due to the pressure differential and the rotation at the neck ring and interstage seals and balance pistons, considerable reaction forces arise during rotor vibration. The boundary conditions at these elements are generally described by a mathematical model, consisting of a stiffness, a damping and a mass matrix, i.e., the rotordynamic coefficients of the seal.

A review of literature reveals that some information about total reaction forces of annular seals is available, but no published full scale measured data on individual coefficients exist. Contemporary theories (refs. 8, 9) were found to be able to predict available measured results for plain surface seals to some extent, but detailed investigations on serrated or grooved surface patterns are missing.

To validate the theory according to Childs and Nordmann, a full scale test rig for neck ring seals was established and operated at typical Reynolds numbers of boiler feed pumps. Skew symmetric stiffness, damping and mass matrices were measured. Rotordynamic coefficients and hydraulic friction factors of a plain and a serrated seal are presented. New ("as built") and worn conditions for the example of a serrated seal are demonstrated.

Comparison of theoretical results (ref. 9) with measured data is shown and indicates a not very satisfying accuracy. Predictions for rotordynamic coefficients are demonstrated to be generally high for stiffnesses, much too low for cross coupled stiffnesses and about twice as large as the measurement errors for direct damping. The other coefficients are negligible, as found from measurement as well as from theory.

2. TEST EQUIPMENT

2.1 Test Machine

The test apparatus uses the housing, support and excitation device from the test rig used previously for impeller interaction measurements as described in (ref. 6). Figure 1 indicates the general arrangement of the test machine. The test rig is dynamically de-coupled from the ground by the heavy base plate. In the drive end view the hydraulic shaker attached to the swinging frame is on the right side of the test machine. This frame contains the rotor bearings and is supported in a pivot on the left side of the test rig. This arrangement provides that any movement of the hydraulic shaker makes the rotor support move around the pivot. As the radius is very large and the vibration amplitudes induced by the shaker are several magnitudes smaller, a linear vertical movement of the rotor relative to the main housing is attained. Tie rods take up the axial thrust of the otherwise axially free rotor support, and hence radial alignment is maintained for any axial forces.

Figure 2 is a general cross section of the test rig. The inlet is marked with an arrow. From the large annulus around the bearing section, the fluid passes the guide vanes and is led radially inwards to the entrance of the seal. It is now forced through the narrow annular gap formed by the seal insert and the rotor. Behind the seal, the fluid is gathered in a large space and leaves the test machine through the exit.

Figure 3 indicates that the design allows easy exchange of stator inserts in order to measure different surface geometries, while the rotor surface remains unchanged. Four temperature compensated proximity probes of the eddy current type are provided to measure effective rotor movement in the radial direction, and four axial probes were installed to monitor rotor tilting. The rotor is attached directly to a calibrated piece of shaft, which is instrumented with strain gauges to measure the reaction forces at the rotor. The rotating disk, the counter part of the seal insert, is hollow. Hence mechanical mass is reduced and measurement errors of inertial forces are minimized. The back side of the rotor is sealed by a radial flow hydrostatic seal, which does not influence lateral forces measurement. 48 guide blades can be turned in any position, -75° to +75° from the radial direction, by means of a connecting chain, controlled from the outside by four axes. The seal insert against the rotor was modelled in a FE analysis to prove that no misalignment of the seal under pressure and temperature occurs.

A detailed cross section of the seal alone can be seen in figure 4. Two sets of static and total pressures are measured immediately in front of the seal entrance at opposite circumferential locations. The tangential velocity of the water entering the seal can be calculated, using measured flow and the continuity equation. The tangential velocity of the water jet leaving the seal can not be measured. Thus, only static pressure is measured here to calculate the total pressure differential.

Static and dynamic properties of the test machine were calculated and optimized. The FE analysis and measurement of the machine showed a critical first mode above 150 Hz in air and, because of the stiffening effect of the annular seal, above 170 Hz in water.

A tilting of the rotor leads to measurement errors. According to theories of Childs (ref. 10) and Fenwick (ref. 11), the displacement tilt divided by the maximum mean displacement may not be larger than some 3% in order to avoid errors larger than 10% for the stiffness measurement:

$$\frac{\bar{F}_x}{Y} = K_{xx}\cdot\left[1 + RK\cdot\frac{\bar{X}_{in} - \bar{X}_{out}}{Y}\right] \qquad \frac{\bar{F}_y}{Y} = K_{yy}\cdot\left[1 + RK\cdot\frac{\bar{Y}_{in} - \bar{Y}_{out}}{Y}\right] \qquad (1)$$

with $RK = f(L_{seal}/h_o)$ being the theoretical correction factor. For the present test rig it is estimated that $RK \approx 3 \div 3.5$.

To estimate tilting errors, an FE calculation has been done, which indicated a strong general dependency of the displacement tilt on the frequency. Maximum calculated displacement tilt in the vertical (Y-) direction is about 9% for smooth and 4.5% for serrated seals. Calculated tilt in the horizontal direction is less than 1%, as the displacement X is very small. Rotor tilting hence had to be monitored by means of axially placed proximity probes. Measurement indicated generally much smaller tilts, and therefore errors in the stiffness were acceptable.

2.2 Test Loop

A key plan of the closed circuit test loop is shown in figure 5. The loop is designed for a maximum temperature of 160 °C and use of demineralized water. Pressure is generated externally, in a Sulzer standard pump, with operating conditions at a best efficiency point of 740 m head at 56 1/s flow. Entrance pressure and flow of the test machine are controlled by valves in the main and the bypass branch. Maximum allowable pressure downstream of the test machine is restricted by the turbine flow meter to 20 bar, enough to prevent vaporization at 160 °C. Combined main and bypass quantities pass partially through the main heat exchanger, depending on the duty point, and are led back to the main pump. System pressure is maintained by a plunger pump, which supplies cooling water for the mechanical seal and the bearings out of a reservoir.

2.3 Instrumentation and Data Acquisition

Dynamic Measurement (ref. 6)

The linear relationship between forces and displacement, of equation (2), is assumed. For rotational symmetry, matrices become skew symmetric and the relation can be written as

$$-\begin{bmatrix} F_x \\ F_y \end{bmatrix} \equiv \begin{bmatrix} K & k_c \\ -k_c & K \end{bmatrix} \cdot \begin{bmatrix} X \\ Y \end{bmatrix} + \begin{bmatrix} C & c_c \\ -c_c & C \end{bmatrix} \cdot \begin{bmatrix} \dot{X} \\ \dot{Y} \end{bmatrix} + \begin{bmatrix} M+M_m & m_c \\ -m_c & M+M_m \end{bmatrix} \cdot \begin{bmatrix} \ddot{X} \\ \ddot{Y} \end{bmatrix} - \begin{bmatrix} F_{xo} \\ F_{yo} \end{bmatrix} \qquad (2)$$

where M_m stands for the mechanical mass of the rotor acting on the calibrated piece of shaft, and F_{xo} and F_{yo} indicate any forces not coherent with the vibration motion. F_{xo} and F_{yo} are only caused by noise of the machine and are small. Synchronous time averaging eliminates the noncoherent forces. As harmonic motion applied, complex notation can be used:

$$X = \mathrm{Re}\cdot\left[\bar{X}\cdot e^{j\Omega t}\right] \qquad F_x = \mathrm{Re}\cdot\left[\bar{F}_x\cdot e^{j\Omega t}\right]$$

$$Y = \mathrm{Re}\cdot\left[\bar{Y}\cdot e^{j\Omega t}\right] \qquad F_y = \mathrm{Re}\cdot\left[\bar{F}_y\cdot e^{j\Omega t}\right] \qquad (3)$$

Introducing equations (3) into (2) yields the impedance functions D and E:

$$-\begin{bmatrix} \bar{F}_x \\ \bar{F}_y \end{bmatrix} = \begin{bmatrix} \bar{D} & \bar{E} \\ -\bar{E} & \bar{D} \end{bmatrix} \cdot \begin{bmatrix} \bar{X} \\ \bar{Y} \end{bmatrix} \qquad (4)$$

which corresponds to

$$\bar{D} = K + j \cdot \Omega \cdot C - \Omega^2 \cdot (M + M_m)$$
$$\bar{E} = k_c + j \cdot \Omega \cdot c_c - \Omega^2 \cdot m_c \qquad (5)$$

Because of the rotational symmetry and the harmonic motion, alternatively the imaginary parts can also be introduced into equation (2), resulting in a 90° rotation of the system. As linear equations are used, both cases can be superimposed. Of importance is the fact that no assumptions about the orbit path are needed to get these equations. Thus any linear movement is appropriate. However, as only displacement in the vertical direction occurs, rotational symmetry must be assumed, and only six individual coefficients can be extracted.

In the frequency domain, the impedance functions D and E consist of a constant term and a term depending on the square of the excitation frequency in the real part. The imaginary part is represented by a linear term in frequency, only. Obviously there is no a priori knowledge that those functions represent the actual physical behaviour of the annular seal, as any polynomial in the exciting frequency of an arbitrary degree could fit the results. Anyhow, for practical reasons the number of coefficients should be as small as possible.

Equations (5) demonstrate the physical meaning of D and E. In figure 6, the reaction forces created by individual stiffness, damping, and mass terms and their direction relative to the displacement and velocity vector are shown.

At any given operating point, measurement of complex forces F_x and F_y and displacements X and Y with several rapid sweeps of excitation frequency determine the impedance functions D and E. Curve fitting the results to the equations (5), yields the stiffness, damping and mass coefficients that are being sought.

Displacement and force signal processing:

Figure 7 shows the signal flow at the test machine. The rotating piece of shaft is equipped with six strain gauges for measurement of six degrees of freedom. The careful static and dynamic loading of this device resulted in a full 6x6 calibration matrix. Signal wires are led through the shaft, the coupling and the gear box into the rotating amplifier. Hence stable bridge supply is provided for, and signals can be amplified to pass the slip ring assembly without loss of information.

Radial displacement is measured in both the horizontal and vertical direction by two temperature compensating eddy current probes. To check the displacement tilt, four axially placed probes measure the tilting angles α and β of the rotor around the x- and y-axis.

The data acquisition system is triggered to the rotational frequency. Sampling starts at a zero degree rotor position, and one data block is filled with 1024 points after 32 revolutions taking 32 samples per revolution. The excitation signal is generated digitally from a data block of 1024 points and is made synchronous to the data sampling by triggering.

Data processing of force and displacement signals is shown in figure 8. After the analog-digital conversion, all signals are averaged. As the excitation signal is phase locked to the rotor position, averaging of 1000 data blocks removes all forces and displacements not coherent to the excitation signal. Forces and moments are then calculated, applying the calibration matrix, and are converted to the stationary reference. No run out compensation is needed for displacement measurements because of the averaging procedure. From α and β, the radial displacement taper can be calculated with the help of some geometrical data.

Signals subsequently undergo a Fourier transform to yield the complex radial displacement and forces in the stationary horizontal and vertical direction. The relative displacement tilt is used to estimate the possible error caused by tilting. Equation (4) finally indicates that the relation between forces and displacements, and impedance functions D and E can be calculated.

To minimize the time of measurement at one operating point, the excitation frequency Ω is varied in a rapid sweep from zero up to about 140% of the running frequency. Some measurements at constant Ω proved that coefficients do not depend on the rapid sweep. Curve fitting of E and D uses only the excitation range from 10% to 120% of the running frequency for accuracy reasons. The running frequency is excluded, to avoid the measurement of geometric tolerance effects. Reliable measurement of one set of stiffness, damping and mass coefficients is thus ensured and needs less than 10 minutes.

Instrumentation for operating conditions:

To compare individual results, operating and boundary conditions must be known. Figure 9 indicates the signal flow for operating conditions. Fluid temperatures in front and behind the seal are measured by two thermoelectric couples. Electric signals are led to a line recorder for a visual check and through the signal conditioning to the data acquisition system.

The pressure of individual locations is led hydraulically to strain gauge type transducers located outside of the machine. This implies that only quasi-static pressure can be measured. Transducers signals are led through signal conditioning to the data acquisition system.

The turbine flow meter yields a flow proportional frequency. This frequency, as well as the measured rotating frequency of the shaft, is not transmitted directly to the data acquisition system. Impulse sampling and averaging takes too much space and time on the computer. Hence, those two results are the only ones to be entered manually.

Signal processing for operating conditions:

Figure 10 shows the processing of the measured operating conditions. Direct readings are treated in the same way as the displacement and force data. The two manually entered frequencies are not subject to sampling and averaging and are multiplied by their calibration factors. Including information about the geometry, all essential operating conditions, including fluid properties, can be derived:

- Rotor speed
- Mean temperature (fluid properties)
- Mean static pressure immediately in front and behind the seal
- Mean pressure drop
- Kinetic pressure (pitot tube used allows for relative flow angles up to at least +/- 25°)
- Mean total velocity in front of seal (kinetic pressure)
- Mean meridional velocity in front of and within seal (continuity)
- Mean circumferential velocity in front of seal
- Friction coefficient (static pressure distribution within seal)

With this information, measured rotordynamic coefficients can be presented in nondimensional diagrams, using the circumferential Re-number as the abscissa and the axial to circumferential Re-number ratio as the parameter. Hydraulic behaviour can be presented correspondingly.

Calibration:

All measurement devices, static as well as dynamic, were calibrated carefully, to ensure reliable results.

The Eigenfrequencies of the system were checked in water. Accordingly, impedance functions match measured data most precisely up to about 100 Hz, and a first resonance appears at some 150 Hz. Maximum excitation frequency required during tests is only about 80 Hz, and no resonance effects take place.

For appropriate measurement, it must be ensured that the rotor vibrates with an approximately constant amplitude over the whole excitation frequency range. Therefore, the chirp signal has to be surveyed and adapted, if necessary. Confirmation took place visually in the time or frequency domain during measurement.

A typical example at 2000 rpm is shown in figure 11. The rapid sweep signal is nicely reproduced in the vertical direction, amplitudes being in the range of a strongly vibrating pump; and the response is quite small in the horizontal direction. The frequency spectrum shows the excitation to span the range from 3 to about 40 Hz with fairly constant resulting displacement. Note that the running frequency is removed and that the signal-to-noise ratio is very good. Figure 12 shows the vertical and horizontal forces. The frequency spectrum of the vertical displacement and force shows a moderately even distribution. If the decrease of displacement with increasing frequency were larger, a linearly or quadratically increasing chirp input would have to be used.

3. MEASURING RANGE AND NONDIMENSIONAL PRESENTATION

3.1 Boundary conditions of test loop and test rig:

There is a physical limitation of the measuring range by the test machine. The following operational limits are encountered:

Maximum at	20	160	[°C]	Restriction by
speed	4000	4000	[rpm]	Electric drive
inlet pressure	75	70	[bar]	Inlet flange
outlet pressure	2	8	[bar]	Avoid vaporization
pressure differ.	55	55	[bar]	Hydrostatic seal

Below 500 rpm data sampling becomes erratic, and a pressure differential below approximately 2 bar yields forces which are too small to be measured reliably. The minimum temperature is close to the temperature of the environment.

3.2 Measuring range:

Boundary conditions for a centrifugal pump in terms of rotor speed and pressure are approximated by the following equations:

$$\frac{p_1}{p_2} = \left[\frac{n_1 \cdot (D_1)}{n_2 \cdot (D_2)} \right]^2 \tag{6}$$

The axial velocity v through the annular seal is about proportional to the square root of the pressure differential as can be derived from equation (7):

$$dp = rho \cdot \frac{v^2}{2} \cdot \left[\frac{Lambda \cdot L_{seal}}{2 \cdot h_o} + Ze_1 + Ze_o \right] \tag{7}$$

Hence v is directly proportional to the running speed. Writing the ratio of axial to circumferential Reynolds number in a seal yields

$$\frac{Re_a}{Re_c} = \frac{v}{\omega \cdot R} \tag{8}$$

As the geometrical dimensions of the seal are directly correlated to the outer diameter D_2 of the impeller, which determines mainly the generated pressure at a certain speed, the scale of the pump can not change the ratio of equation (8). Thus the ratio of the axial to the circumferential Reynolds number must lie in a narrow range:

$$\frac{Re_a}{Re_c} = 0.45 \div 0.95 \tag{9}$$

The range given here is applicable for specific speeds according to boiler feed pumps. For very high specific speed impellers the ratio may become lower.

With this insight, the measuring range can be defined as shown typically in figure 13. Axial and circumferential Reynolds numbers were selected as three fixed ratios, 0.3, 0.6 and 0.9. Six speeds resulting in Re_c's from 20'000 to 280'000 are chosen. Re_a reaches from 6'000 to about 220'000, depending on each Re_c. The large Reynolds number range was attained by varying temperatures from 20 to 160 °C. A summary of operating conditions is shown in figure 14.

Inlet swirl:

With the adjustable guide vanes used, any attainable inlet swirl remains lower than in a pump. Water exiting an impeller has a high circumferential velocity component. This velocity increases as the medium flows radially inwards, reaching a U_{tho} of about 0.7 ÷ 0.8 at the entrance of the seal. Using guide vanes, a maximum of about U_{tho} = 0.15 can be reached, if the whole Re_a range is to be measured at constant U_{tho}.

For direct comparison of coefficients at individual Re-ratios, the inlet swirl has to be approximately equal for all ratios measured. To get detailed information about the influence of inlet swirl on rotordynamic coefficients, a variation from negative to maximum positive pre-rotations was measured at four selected operating points, where the highest inlet swirls can be attained. Results confirm that this procedure provides sufficient information for the extrapolation of coefficients to more realistic inlet swirls.

3.3 Test program and specifications:

The three seal configurations to be discussed are shown in figure 15. The nominal mean diametric seal clearance varies generally from about 0.15 to 0.3% of the seal diameter, depending on the absolute size and the application of the pump, and is doubled for the "worn condition." The seal diameter of 350 mm corresponds approximately to an impeller diameter $D_2 \approx 500$ mm.

Results of a smooth seal and a serrated seal with nominal and twice nominal clearance are presented. Yet, there is still a huge variety of other interesting configurations. All geometries, including some further variants, have been measured under EPRI (Electric Power Research Institute Inc., Palo Alto CA, USA) contract RP 1884-10.

3.4 Nondimensional presentation:

The general definition must include the pressure differential, the radius, the seal clearance, the length and, partially, the angular rotor speed to produce literally nondimensional coefficients. Whether the coefficients depend linearly or by any exponent on those parameters can not be concluded explicitly. Hence, the following definitions are used:

$$F_r^* = \frac{F_r/e \cdot ho}{L_{seal} \cdot R \cdot dp} \qquad F_t^* = \frac{F_t/e \cdot ho}{L_{seal} \cdot R \cdot dp}$$

$$K^* = \frac{K \cdot ho}{L_{seal} \cdot R \cdot dp} \qquad k_c^* = \frac{k_c \cdot ho}{L_{seal} \cdot R \cdot dp} \tag{10}$$

$$C^* = \frac{C \cdot ho \cdot \omega}{L_{seal} \cdot R \cdot dp} \qquad c_c^* = \frac{c_c \cdot ho \cdot \omega}{L_{seal} \cdot R \cdot dp}$$

$$M^* = \frac{M \cdot ho \cdot \omega^2}{L_{seal} \cdot R \cdot dp} \qquad m_c^* = \frac{m_c \cdot ho \cdot \omega^2}{L_{seal} \cdot R \cdot dp}$$

Experience with measured data exhibited that normalized rotordynamic coefficients become almost constant against both Re_a and Re_c at constant Re_a to Re_c ratios. This allows a huge amount of information to be condensed by plotting the mean values as bar charts at individual Re-ratios.

Radial and tangential forces can be deduced from equations (2). For a circular vibration orbit with radius e, the displacement, velocity and acceleration vectors become

$$\begin{bmatrix} X \\ Y \end{bmatrix} = \begin{bmatrix} e \cdot \cos(\Omega \cdot t) \\ e \cdot \sin(\Omega \cdot t) \end{bmatrix} \quad \begin{bmatrix} \dot{X} \\ \dot{Y} \end{bmatrix} = \begin{bmatrix} -e \cdot \Omega \cdot \sin(\Omega \cdot t) \\ e \cdot \Omega \cdot \cos(\Omega \cdot t) \end{bmatrix} \quad \begin{bmatrix} \ddot{X} \\ \ddot{Y} \end{bmatrix} = \begin{bmatrix} -e \cdot \Omega^2 \cdot \cos(\Omega \cdot t) \\ -e \cdot \Omega^2 \cdot \sin(\Omega \cdot t) \end{bmatrix} \tag{11}$$

Because of the circular symmetry, no phase angle is needed. The simplest case to calculate radial and tangential forces is at $t = 0$, where $\sin(\Omega \cdot t) = 0$ and the eccentricity is on the x-axis. Hence, F_x becomes F_r and F_y becomes F_t, and the matrix equation (12) can be rewritten as

$$\begin{aligned} -F_r &= K \cdot e + c_c \cdot e \cdot \Omega - M \cdot e \cdot \Omega^2 \\ -F &= -k_c \cdot e + C \cdot e \cdot \Omega + m_c \cdot e \cdot \Omega^2 \end{aligned} \tag{12}$$

Introducing the normalization of equations (10) into equations (12), the following dimensionless presentation is found:

$$\begin{aligned} -F_r^* &= K^* + c_c^* \cdot \left[\frac{\Omega}{\omega}\right] - M^* \cdot \left[\frac{\Omega}{\omega}\right]^2 \\ -F_t^* &= -k_c^* + C^* \cdot \left[\frac{\Omega}{\omega}\right] + m_c^* \cdot \left[\frac{\Omega}{\omega}\right]^2 \end{aligned} \tag{13}$$

Radial and tangential forces are only plotted at one selected ratio of excitation to running frequency, 0.8, as typical ratios for instabilities at high

energy pumps range from about 0.7 to 0.9 (ref. 1). The same scheme as for coefficients is used.

4. MEASURED DATA

4.1 Error Estimation:

High radial stiffness of the measuring shaft, which is attained with a short and compact shape, is required in order to avoid critical speeds. This implies that the measuring system was very susceptible to nonsymmetrical stress distributions. Based on experience, the maximum uncertainty of the dynamic forces is estimated to be ±5%. The uncertainties of the displacement measurement are measured to be within ±2%. The signal conditioning and processing are further sources of deviations. Therefore the accuracy of the measured impedance functions is estimated to be within ±10% (worst case).

The accuracy of the extracted coefficients depends further on the scatter of the measured values and on the deviation of the actual impedance function from the underlying mathematical model. Some of the uncertainties mentioned are absolute values, and thus, the relative measurement errors are quite small for large absolute loads and become large for values close to zero!

Standard deviations of measured data indicate clearly that the direct stiffness and damping coefficients, being the largest values, are matched very well. The cross coupled stiffness is still fairly accurate, results are better with larger inlet swirls and hence, larger absolute coupled stiffnesses. The direct mass at low Reynolds number ratios exhibits satisfactory relative standard deviations. Cross coupled damping and mass terms as well as direct mass terms at higher Re-ratio values can not be considered reliable at all.

For the nondimensional presentation, the errors of the operating conditions need to be known. The mean static pressure measurement was found to vary within ±5%. The accuracy of the pressure transducers lies within 2% (including static drifts), and the flow meter gives results with less than 1% error. The rotor speed is assumed to be erratic by some 2%. The fluid properties are estimated to be within 2% of their true values and geometrical data is judged to be within 5% of the actual dimensions under load and temperature. Those errors add up statistically to possible deviations from operating conditions of approximately 8%. Additionally, for the cross-coupled stiffness, the error of the circumferential inlet velocity, which is about 5%, must be included, as k_c^* varies about linearly with U_{tho}. This results in slightly larger deviations of 9% for the coupled stiffness.

Together with the estimated maximum load measurement error of ±10% and individual deviations from impedance functions, this leads to the following worst case uncertainties of nondimensional rotordynamic coefficients:

K^*: ≈ ± 13 %	k_c^*: ≈ ± 16 %
C^*: ≈ ± 13 %	c_c^*: ≈ ± 41 %
M^*: ≈ ± 14 % (min.)	m_c^*: ≈ ± 115 %
M^*: ≈ ± 21 % (mean Re-ratio)	
M^*: ≈ ± 56 % (max.)	

Hence, only stiffness coefficients, the direct damping and the direct mass term at smallest Re-ratios are reliable results, but coefficients with large possible errors are of no interest, as their actions on the rotor are negligible.

4.2 Discussion of Test Results:

In order to discuss the test results, bar diagrams have been established. The total average of all points at all Re-ratios reflects whether the test result depends on the individual Re-ratios or not.

Rotordynamic coefficients: (Figures 16 through 19)

OOS:

The smooth, N8 surface roughness seal is shown in figure 16. The direct stiffness exhibits scatter well within the limits of measurement errors, and the nondimensional stiffness of this test series is constant for all Reynolds numbers and for any Re-ratio.

The cross coupled stiffness indicates a dependency on the Re-ratio, but not on the Re-level. Extracted cross coupled stiffnesses were all within the band width of estimated measurement error, even in spite of some inlet swirl variations. For a constant inlet swirl, the cross coupled stiffness decreases with increasing Re-ratios. At higher Re-ratios, the time needed to pass through the seal clearance becomes relatively shorter and, as a consequence, the fluid can not be accelerated in the circumferential direction to the same extent as with lower Re-ratios. However, for this test series the inlet swirl used for individual Re-ratios increased with the Re-ratio, and both effects compensate to some degree.

The direct damping depends on the Re-ratio, too. Yet, at individual Re-ratios, coefficients remain constant over the total Re-range measured, and scatter lies well within the estimated relative error. Cross coupled damping seems to exist at the lowest Re_a/Re_c only. As it is very small, scatter is considerable, and at higher Re-ratios, c_{xy}^* is essentially zero.

The direct mass term exists at lowest Re-ratios, but the relative scatter is considerable and larger than estimated errors. A distinct decrease can be found for increasing Re-ratios. Averaged cross coupled mass coefficients are not reliable at all, as they are practically nonexistent for short seals.

At the chosen whirl frequency ratio of 0.8 (vibration to running frequency), the re-composed radial and tangential forces exhibit constant averaged values at individual Re-ratios, including little relative scatter. The centering radial forces do not depend on the Re-ratios and the tangential forces are braking, though to a lesser extent for higher Re-ratios. The gradient of tangential forces would be smaller or inverted if the attainable inlet swirl, and hence the cross coupled stiffness, were at realistic values of a pump neck ring seal. The cross coupled stiffness can be linearly extrapolated with the inlet swirl, including a parallel offset towards positive inlet swirls, see figure 19. The definition of this straight line as well as numeric values of slopes and offsets for individual configurations and Re-ratios can be found in table 3 of the appendix. Extrapolation to an $U_{tho} = 0.75$ results in all tangential forces becoming driving and diminishing in absolute magnitude with increasing Re-ratios, see overview of extrapolated F_t^*

in table 2. The fact that all extrapolated F_t^* include much larger errors, i.e., approximately ±30%, than estimated for measured values must be stressed.

04S:

Figure 17 presents average values for the N8 surface roughness, serrated seal. Comparison with the smooth seal indicates no drop of the total averaged dimensionless stiffness for the serrated seal. However, for the serrated seal, K_{xx}^* is not entirely constant with Re-ratios and individual differences of the average stiffnesses up to some 10%.

The cross coupled stiffness is reduced considerably in comparison to the values for the smooth seal, but direct damping terms are a little higher than the values of the smooth seal. At the present moderate inlet swirl, the combination of the more advantageous damping and coupled stiffness coefficients from the serrated seal leads to a moderate gain in braking forces around 20%. The extrapolation shown in figures 2 and 3 indicates clearly the driving tendencies at realistic inlet swirls for both smooth and serrated seals. However, the serrated seal is extensively less destabilizing at low Re-ratios; though this advantage diminishes towards high Re-ratios.

04D-M:

Average values of the double clearance, "worn" serrated seal are presented in figure 18. In this configuration the serration depth is reduced from the "new" condition in order to simulate wear, which occurs on both rotor and stator.

The direct stiffness is not quite inversely proportional to the seal clearance, as the definition of nondimensional coefficients would suggest, resulting in higher dimensionless values for the worn condition. A similar slight decrease of nondimensional direct stiffness with increasing Re-ratios as with the single clearance seal is found.

The cross coupled stiffness is approximately inversely proportional to the seal clearance. The averages of the single and double clearance seals are not exactly equal, but scatter of the double clearance seal is notably large at the lowest force levels, and the average of the single clearance seal fits well enough into this band of standard deviations. However, the drop of cross coupled stiffness with increasing Re-ratios is slightly larger for the double clearance seal.

Nondimensional direct damping at low Re-ratios does not confirm the definition equation (10) with respect to seal clearance. As damping of the double clearance seal drops more extensively with Re-ratios, the nondimensional damping values from test series 04D and 04S match better at higher Re-ratios.

The nondimensional mass is approximately twice as large as for the single clearance seal, i.e., the mass becomes more significant for the resulting radial force. Where the nondimensional, direct stiffness is almost 50% higher for the double clearance seal, the associated radial force is only little more than 35% higher. However, the acting dimensional radial force is only about half as large for the 04D series seal, as F_r^* is divided by the double clearance and multiplied by a smaller pressure differential than for the single clearance seal.

The nondimensional tangential force becomes distinctively higher for the double clearance at the lowest Re-ratios because of the high direct damping. At medium and high Re-ratios, there is no gain in the nondimensional tangential force. Values

extrapolated to higher inlet swirls are shown in table 2. Driving dimensionless tangential forces are smaller for the "worn" seal than for the "new" seal. However, the advantage of the "worn" seal being less destabilizing than the "new" seal diminishes with increasing inlet swirl and increasing Re-ratio.

Note that F_t^* of the "worn" seal is approximately one order of magnitude smaller than its two components and that the cross coupled stiffness is very uncertain because of large extrapolation. This implies the possibility of a large relative error of F_t^*.

Well designed swirl breaks cut the inlet swirl to approximately $U_{tho} = 0.4$, and hence, both seal conditions become stabilizing. However, the stabilizing effect of the worn seal will be smaller than the one of the new seal, as the lower pressure drop and the double clearance will result in an approximately 60% smaller dimensional force (see equations (10)).

Flow Resistance: (Figure 20)

Some average values, mainly at low Re-ratio, may not be representative for the friction behaviour, indicated by the large standard deviations. This is not measurement scatter, but the change of the friction factor with Reynolds numbers' which is larger for Lambda values than for rotordynamic coefficients. However, to get a general overview, and in order to compare individual configurations, these charts are very useful.

The bar charts provided are only comparable to each other if measured Re-ranges are approximately equal or if the standard variation indicates constant Lambda values. Re-ranges are the same for the nominal clearance seals, and slightly higher for the double clearance seal. However, the double clearance seal provides quite constant Lambda values at a moderately higher Reynolds number (a factor of 2) in contrast to the Re-range of $Re_{max}/Re_{min} \approx 13$.

A high surface roughness of N8 yields quite large friction factors, the equivalent relative roughness is found to be around 0.02 from the comparison of the smooth seal with the Moody diagram. Indeed, comparison with another measurement at Sulzer Brothers, as published in (ref. 12) and (ref. 13), proves the growth of friction factors from N6 to N8 surfaces to be considerable.

The decrease of Lambda values is largest with increasing Re_a's at lowest Re-ratios and becomes quite small at higher Re-ratios. Furthermore, inlet swirl does not affect the friction factor. Increased leakage flow with swirl breaks hence results exclusively from the lower pressure drop within the impeller side room, caused by the lowering of the rotational velocity, which results in a higher pressure differential across the seal.

Comparison of the serrated seal with the smooth seal shows that there is some gain in friction factors at low Reynolds number, and a definitive increase of Lambda values is attained at higher Re-numbers. For high Re-numbers, the increase is considerable around 30%. From a hydraulic point of view, a high surface roughness is desirable, even with serrated seals. Additionally, the serration geometry might be further optimized, in order to result in higher friction. However, further gain in friction must be compared to the changes in rotordynamic behaviour.

Wear of the serrated seal, as it is simulated with test series 04D indicates, that friction factors rise marginally when the clearance is opened to twice its original value and the serration depth is reduced. Realize that, even for a slightly increased Lambda value, the leakage flow does increase quite drastically with larger seal clearances and hence, Reynolds numbers become larger.

5. CONCLUSIONS

Rotordynamic and hydraulic annular pump seal coefficients of three typical neck ring configurations have been measured at an accuracy for relevant coefficients within less than ±20%. A smooth seal and a serrated seal in new and worn conditions, have been successfully investigated. The effect of surface roughnesses on friction factors for a smooth seal have been discussed. Operating conditions of full size boiler feed pumps were attained. Restrictions were encountered only in the inlet swirl. Normalization and type of presentation for rotordynamic coefficients have proven to be adequate, resulting in constant values over the Reynolds range measured.

The investigation revealed that, from the skew symmetric 2x2 stiffness, damping, and mass matrices used in the present model for interaction forces, the cross coupled damping and the cross coupled mass terms are totally irrelevant. Considerable direct mass terms occur only at very low ratios of axial to circumferential Reynolds numbers. Even the largest mass coefficients change the radial interaction force of an annular seal only by some 10%. Hence, the size of direct mass terms is merely of secondary importance.

In tables 1 through 4, a rough overview of nondimensional interaction forces, including extrapolation of tangential forces, and averaged friction factors of the three configurations is given. However, normalization for rotordynamic and hydraulic coefficients overestimates the influence of the seal clearance. Double clearance values generally tend to be higher than the related single clearance values.

Damping Action:

The driving tangential force is influenced strongest by individual seal configurations at lowest Reynolds number ratios (table 2). All neck ring seals measured resulted in definitively destabilizing tangential forces at realistic inlet swirls (0.7 ÷ 0.8). The serrated seal (04S) exhibits clearly less destabilizing tendencies than the smooth seal (00S). The advantage becomes smaller with increasing Re-ratios, as the influence of the seal surfaces on the circumferential fluid velocity becomes smaller with the shorter passage time. Double clearance seals can reduce the nondimensional driving tangential force, if properly designed (04D). However, with the use of swirl breaks at neck rings or at interstage bushings, where the inlet swirl is zero, only single clearance seals can provide damping action.

Tangential forces can not be compared directly with the earlier measurements as cited in (ref. 12) and (ref. 13), as only a synchronous excitation was available there. The Re-range in those papers is much smaller and no individual coefficients could be measured. Additionally, the inlet swirl available there was quite different from the present ones. However, taking these uncertainties into account,

damping action as presented in (ref. 13), figure 19, compares fairly well to present results measured at medium Re-ratio and lowest Reynolds numbers.

Stiffening Action:

For individual seal designs, the relative changes of radial forces, i.e., primarily of direct stiffness coefficients, are generally lower than for tangential forces, see table 1. It is remarkable that the stiffening effect is not much lowered for the serrated seal. The increase of dimensionless radial forces of the double clearance seal proves that the clearance in the normalization equations is overestimated. Yet, dimensional stiffening effects of worn seals under normal operating conditions in a pump will definitively be lowered, though to more than only half the magnitude of single clearance seals.

Results of radial forces for the serrated seal compare even better than for tangential forces with measurements as presented in (refs. 12, 13). As the direct stiffness is predominant in the radial force and as it does not depend on inlet swirl, individual excitation frequencies and inlet swirls do not affect the comparison.

Flow Resistance:

Averaged Lambda values as are presented in table 4, need to be interpreted very carefully. Generally, friction factors of smooth surfaces do vary considerably in the Re-range measured for these tests (20'000 ÷ 260'000). However, for the present large relative roughnesses (appr. 0.02, according to Moody's diagram), Lambda coefficients become almost constant at moderate Reynolds numbers. Hence, average values are comparable.

The increase of surface roughness from N6 to the actual N8, results in a distinct rise in flow resistance, as has been found by comparison with results from earlier measurement. The measured serrated seal (04S) exhibits very favourable flow resistance when compared to the smooth seal. It shows considerable gain in friction at low Re-numbers, and the greatest improvement is encountered at the largest Re-numbers. Simulated wear reveals slightly higher friction factors, in spite of higher Re-numbers. However, better hydraulic performance could certainly be attained, for example, by a very deep serration and a high ratio of serration to land width. This advantage might be quickly reduced, as the remaining land portions tend to be worn off sooner than wider land portions. Additionally, such a hydraulically optimized serration pattern deteriorates rotordynamic behaviour because of the large serration depth ("Antilomakin" seal).

Final Discussion:

The comparison of rotordynamic and hydraulic coefficients of smooth versus serrated seals clarified that configurations with advantages in one respect may have disadvantages in other respects. However, the presented serrated seal with a surface roughness of N8 is quite favourable in respect to damping capabilities (tangential forces) and exhibits an appealing stiffening effect. Moreover, it displays a fairly high flow resistance.

Obviously, the choice of an appropriate seal configuration depends on the application of the pump, i.e., on whether hydraulic or rotordynamic behaviour is more essential (ref. 14). In any case, rotordynamic behaviour in a boiler feed pump

must be thoroughly considered, when using stepped or deeply serrated anti-stiffness seals in order to gain increased efficiencies.

Unquestionably, not all possible, not even all promising seal configurations have been measured and presented here. One serrated seal has been chosen to be measured in detail, i.e., in new and worn conditions, and has been compared to a plain smooth seal. However, results of the serrated seal measurements are quite attractive, and the serration configuration might be optimized by further investigations.

6. TABLES: SUMMARY OF ROTORDYNAMIC AND HYDRAULIC BEHAVIOUR

Table 1. - SUMMARY OF F_r^*
[frequency ratio 0.8]

Test series:	Fr*:			Re-ratio:		
	a	b	c	a	b	c
00S-V	-0.45	-0.46	-0.44	0.32	0.63	0.94
04S-V	-0.45	-0.43	-0.40	0.32	0.63	0.92
04D-V	-0.63	-0.57	-0.59	0.31	0.62	0.93

Table 2. - SUMMARY OF EXTRAPOLATED F_t^*
[U_{tho} = 0.75 frequency ratio 0.8]
(Ft* < 0: braking, Ft* > 0: driving)

Test series:	Ft*:			Re-ratio:		
	a	b	c	a	b	c
00S-V	+0.31	+0.15	+0.10	0.32	0.63	0.94
04S-V	+0.12	+0.12	+0.10	0.32	0.63	0.92
04D-V	+0.04	+0.05	+0.09	0.31	0.62	0.93

Table 3. - EXTRAPOLATION FOR k_c^*, F_t^* AND CRITICAL FREQUENCY RATIO
Note: all values concerning k_c^* are extrapolated!

$$k_c^* = (U_{tho} - x_o) \cdot m$$

$$F_t^* = k_c^* - \Omega/\omega \cdot C^*$$

Critical frequency ratio for $F_t^* = 0$ (change from braking to driving):

$$(\Omega/\omega)_c = (U_{tho} - x_o) \cdot m / C^* = a \cdot U_{tho} - b$$

Test Series:	Re-ratio: [Re_a/Re_c]	x_o [U_{tho}]	m [k_c^*/U_{tho}]	C^* [-]	a [-]	b [-]	$(\Omega/\omega)_c$ U_{tho}=.75
00S-V	0.32*)	0.0	1.04	0.59	1.76	0.00	1.32
	0.63	0.025	0.59	0.35	1.69	0.04	1.23
	0.94	0.05	0.38	0.21	1.81	0.09	1.26
04S-V	0.32*)	0.06	0.87	0.60	1.45	0.085	1.00
	0.63	0.075	0.61	0.36	1.69	0.125	1.14
	0.92	0.09	0.44	0.24	1.83	0.165	1.21
04D-V	0.32*)	0.07	1.04	0.84	1.24	0.085	0.85
	0.61	0.095	0.57	0.40	1.42	0.135	0.93
	0.92	0.12	0.48	0.27	1.78	0.215	1.12

*) roughly estimated (from individual measurement points)

Table 4. - SUMMARY OF LAMBDA (GENERAL OVERVIEW)

Test series:	LAMB-EFF			Re-ratio:		
	a	b	c	a	b	c
00S-V	0.066	0.055	0.057	0.32	0.63	0.94
04S-V	0.071	0.069	0.074	0.32	0.63	0.92
04D-V 1)	0.076	0.071	0.073	0.31	0.62	0.93

The following restrictions have to be observed, when comparing above averaged friction factors:

1) Higher Re-range at double clearance seals:
no large effect, as Lambda values of serrated double clearance seals do not vary extensively when doubling Re-numbers

7. LIST OF SYMBOLS

Roman:

b	[m]	seal groove width
C	[Ns/m]	symmetric direct damping coefficient
c	[m/s]	total velocity
c_c	[Ns/m]	skew-symmetric cross-coupled damping coefficient
D_s	[m]	seal diameter (general)
D_2	[m]	outer diameter of impeller
D_h	[m]	hydraulic diameter
dp	[N/m²]	total pressure differential across seal
$\underline{D}$	[N/m]	impedance function, definition in equation (4) and (5)
$\underline{E}$	[N/m]	impedance function, definition in equation (4) and (5)
e	[m]	eccentricity
F_r	[N]	force in radial direction
F_t	[N]	force in tangential direction
F_x	[N]	force in x-direction
$\underline{F_x}$	[N]	complex force in x-direction
F_y	[N]	force in y-direction
$\underline{F_y}$	[N]	complex force in y-direction
h_o	[m]	mean seal gap width
K	[N/m]	symmetric direct stiffness coefficient
k_c	[N/m]	skew-symmetric cross-coupled stiffness coefficient
k_s	[m]	equivalent surface roughness
Lambda	[-]	Friction coefficient, see equation (7)
L_{seal}	[m]	seal length
M	[kg]	symmetric direct mass coefficient
m_c	[kg]	skew-symmetric cross coupled mass coefficient
n	[rpm]	rotor speed
nue	[m²/s]	kinematic viscosity
p	[N/m²]	pressure
p_1	[N/m²]	pressure at inlet of seal
p_o	[N/m²]	pressure at outlet of seal
$p(0)$	[N/m²]	pressure at z = 0, within seal
$p(L)$	[N/m²]	pressure at z = L_{seal}, within seal
R	[m]	seal radius R = $D_s/2$

Re	[-]	total Reynolds number, $Re = c \cdot 2 \cdot h_o / nue$
Re_a	[-]	axial Reynolds number, $Re_a = v \cdot 2 \cdot h_o / nue$
Re_c	[-]	circumferential Reynolds number, $Re_c = R \cdot \omega \cdot 2 \cdot h_o / nue$
rho	[kg/m³]	density
t	[s]	time
u	[m/s]	tangential velocity
U_{tho}	[-]	dimensionless tangential velocity, $U_{tho} = u/(R \cdot \omega)$
v	[m/s]	axial velocity
X	[m]	measured horizontal displacement
$\underline{X}$	[m]	complex measured horizontal displacement
Y	[m]	measured vertical displacement
$\underline{Y}$	[m]	complex measured vertical displacement
z	[m]	general axial co-ordinate
Ze_i	[-]	pressure loss coefficient at inlet of seal
Ze_o	[-]	pressure loss coefficient at outlet of seal

Greek:

ε	[-]	relative eccentricity e/h_o
Ω	[rad/s]	angular frequency of excitation
ω	[rad/s]	angular frequency of rotor

Superscripts:

*	dimensionless value

Subscripts:

i	inlet
o	outlet
R	Rotor
S	Stator

8. REFERENCES

1. Pace, S.E., Florjancic, S. and Bolleter, U.: Rotordynamic Developments for High Speed Multistage Pumps. Proceedings, 3rd International Pump Symposium, Houston Texas, May 1986.

2. MADYN, Ing. Büro Klement, Alkmaarstr. 37, 6100 Darmstadt 13, W. Germany or TURBO, University of Kaiserslautern, Pfaffenbergstrasse, 6750 Kaiserslautern, W.Germany and others.

3. Orcutt, F.K.: The Steady State and Dynamic Characteristics of a Full Circular Bearing and a Partial Arc Bearing in the Laminar and Turbulent Flow Regimes. Journal of Lubricating Technology, April 1967.

4. Glienicke, J.: Experimentelle Ermittlung der statischen und dynamischen Eigenschaften von Gleitlagern für schnellaufende Wellen. Forschungsberichte VDI-Z Reihe 1, 22, 1970.

5. Lund, J.E. and Thompson, K.K.: A Calculation Method and Data for the Dynamic Coefficients of Oil-lubricated Journal Bearings: Topics in Fluid Film Bearing and Rotor Bearing System Design and Optimisation. ASME, p. 1, 1978.

6. Bolleter, U. and Wyss, A.: Measurement of Hydrodynamic Interaction Matrices of Boiler Feed Pump Impellers. ASME 85-DET-148, 1985.

7. Bolleter, U., Leibundgut, E. and Stürchler, R.: Hydraulic Interaction and Excitation Forces of High Head Pump Impellers. Proceedings of the 3rd Joint ASCE/ASME Mechanics Conference: Pumping Machinery Symposium, San Diego, July 1989.

8. Childs, D.W.: Finite Length Solution for Rotordynamic Coefficients of Turbulent Annular Seals. ASME Transaction Journal of Lubrication Technology, pp. 437-444, Vol. 105, July 1983.

9. Nordmann, R., Dietzen, F.J., Janson, W., Frei, A., Florjancic, S.: Rotordynamic Coefficients and Leakage Flow of Parallel Grooved Seals and Smooth Seals. Fourth Workshop on Rotordynamic Instability Problems in High-Performance Turbomachinery, Texas A&M University, June 1986.

10. Childs, D.W.: Rotordynamic Moment Coefficients for Finite Length Turbulent Seals. IFTOM Conference on Rotordynamic Problems in Power Plants, Rome, Italy, 28.9-1.10 1982.

11. Fenwick, J., DiJulio, R., Ek, M.C., Ehrgott, R., Green, H. and Shaolian, S.: Linear Force and Moment Equations for an Annular Smooth Shaft Seal Perturbed Both Angularly and Laterally. Proceedings of 2nd Workshop of Rotor Instability at Texas A&M University, NASA Contract NAS8-27980.

12. Florjancic, S. and Frei, A.: Bedeutung der Spaltströmung für die Rotordynamik. Proceedings of the 16. Konstruktions-Symposium der DECHEMA, Frankfurt, June 87.

13. Florjancic, S. and Frei, A.: Dichtspaltströmung in Pumpen: Bedeutung für die Rotordynamik und theoretische Betrachtungen. Proceedings of the Pumpentagung Karlsruhe, Oct. 88.

14. Florjancic, D. and Florjancic, S.: Hydraulic and Rotordynamic Influence on the Choice of Different Pump Types. Proceedings of the Conference on Hydraulic Machinery 88, Ljubljana, Sept. 88.

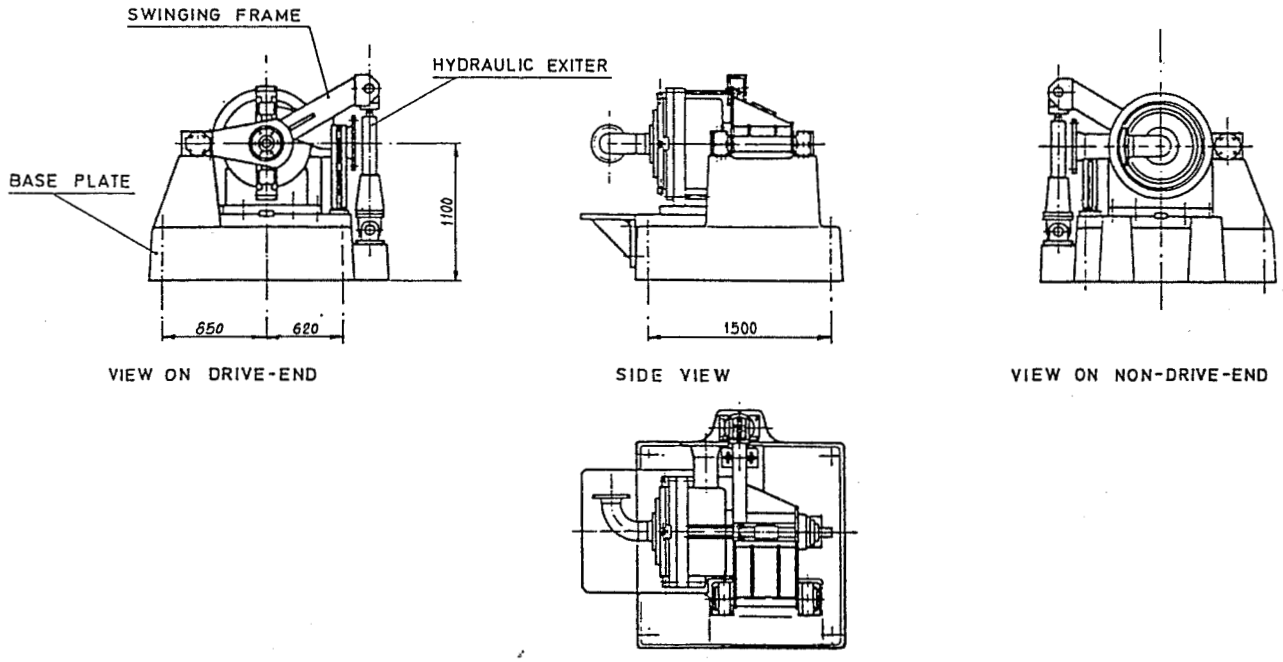

Figure 1. - Arrangement of test machine.

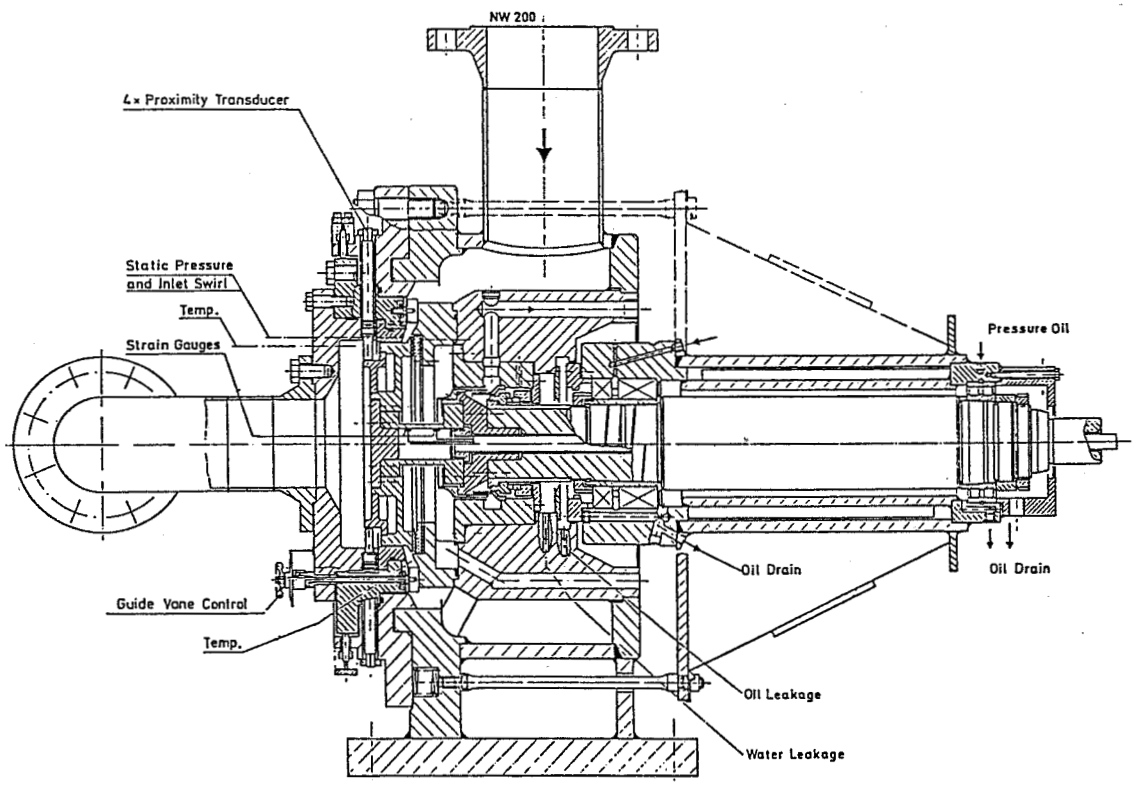

Figure 2. - Cross section of test machine.

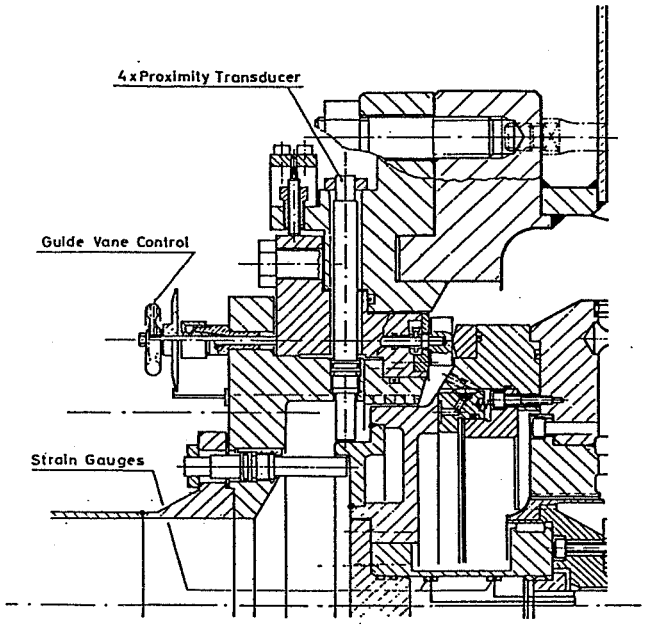

Figure 3. - Rotor, seal and guide vanes, hydrostatic balancing seal.

Straight seal:

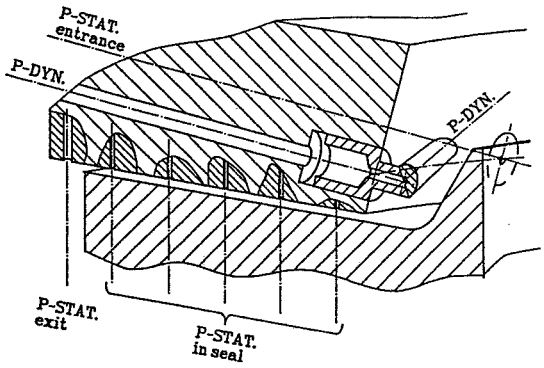

Figure 4. - Detailed cross-section at seal.

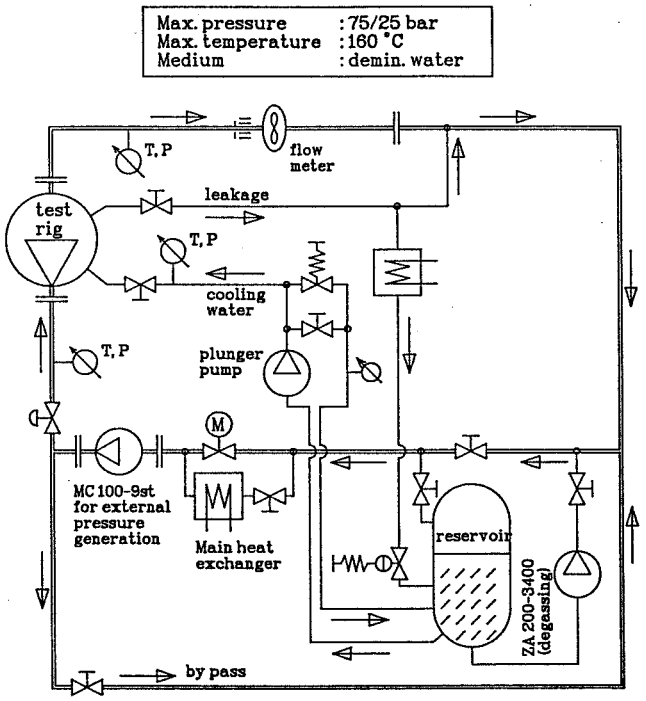

Figure 5. - Test loop.

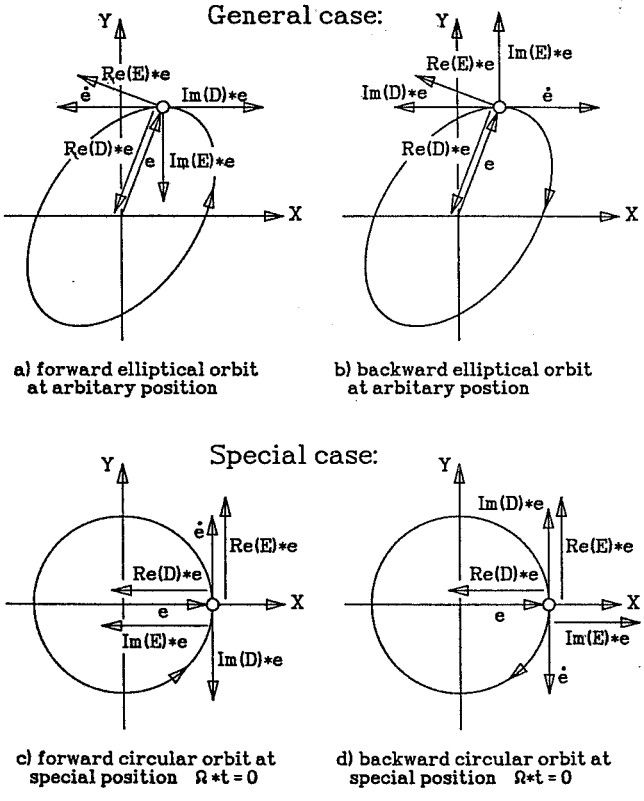

Figure 6. - Physical explanation of impedance functions.

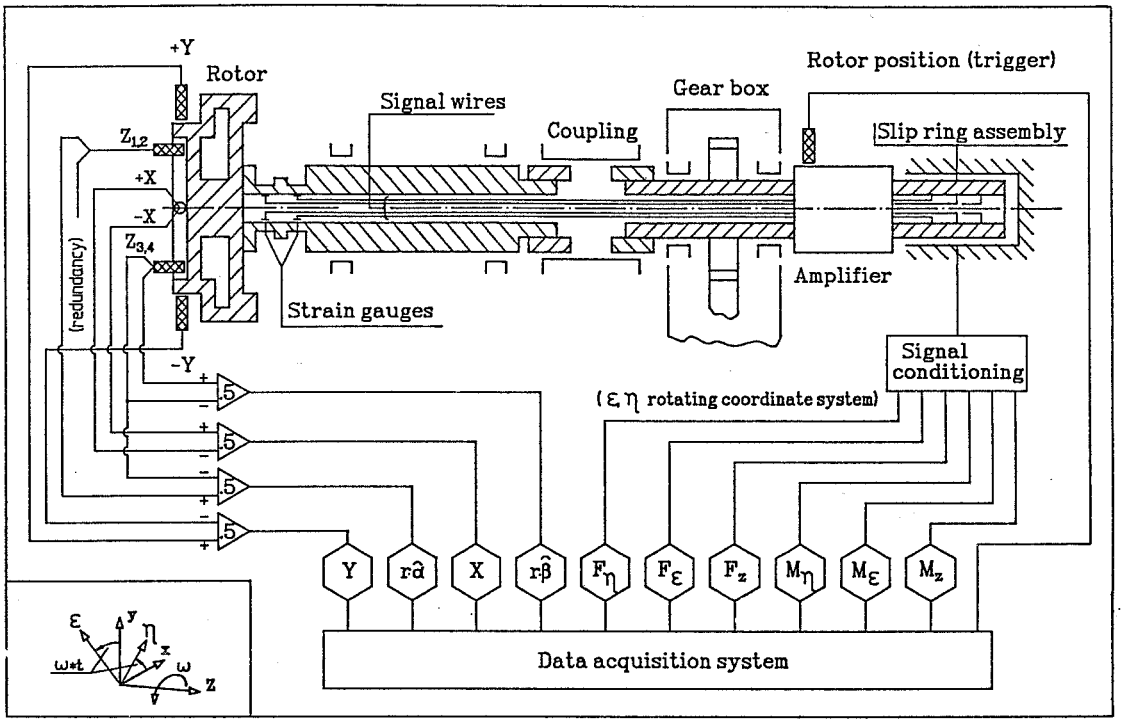

Figure 7. - Signal flow diagram.

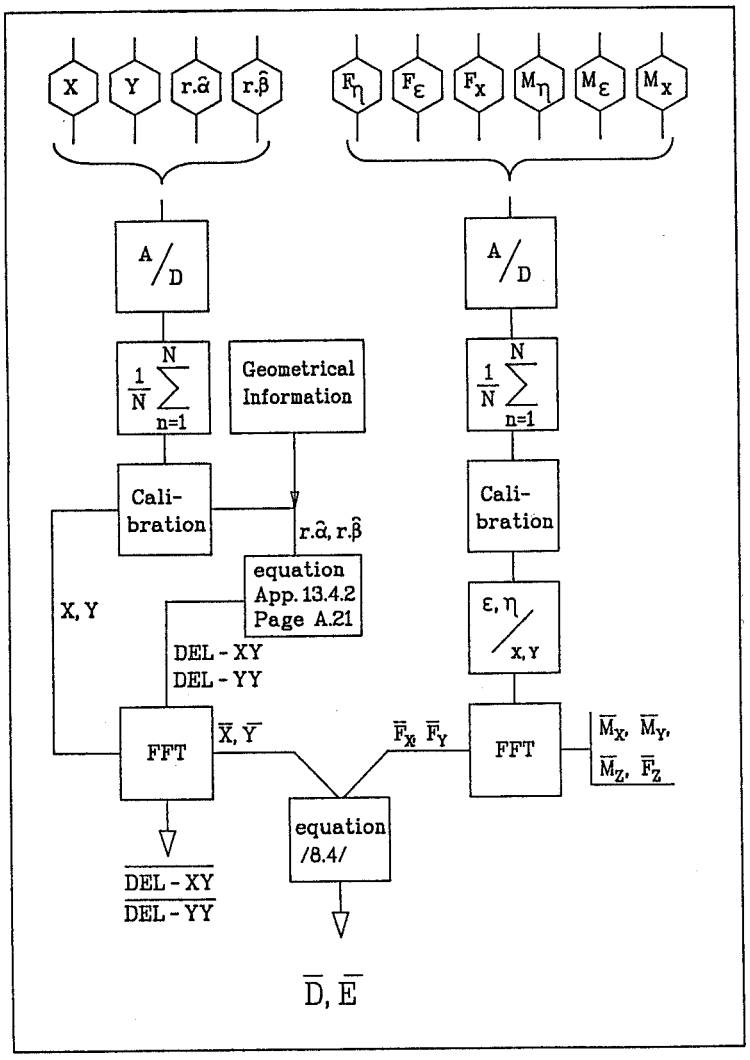

Figure 8. - Signal processing (impedance functions).

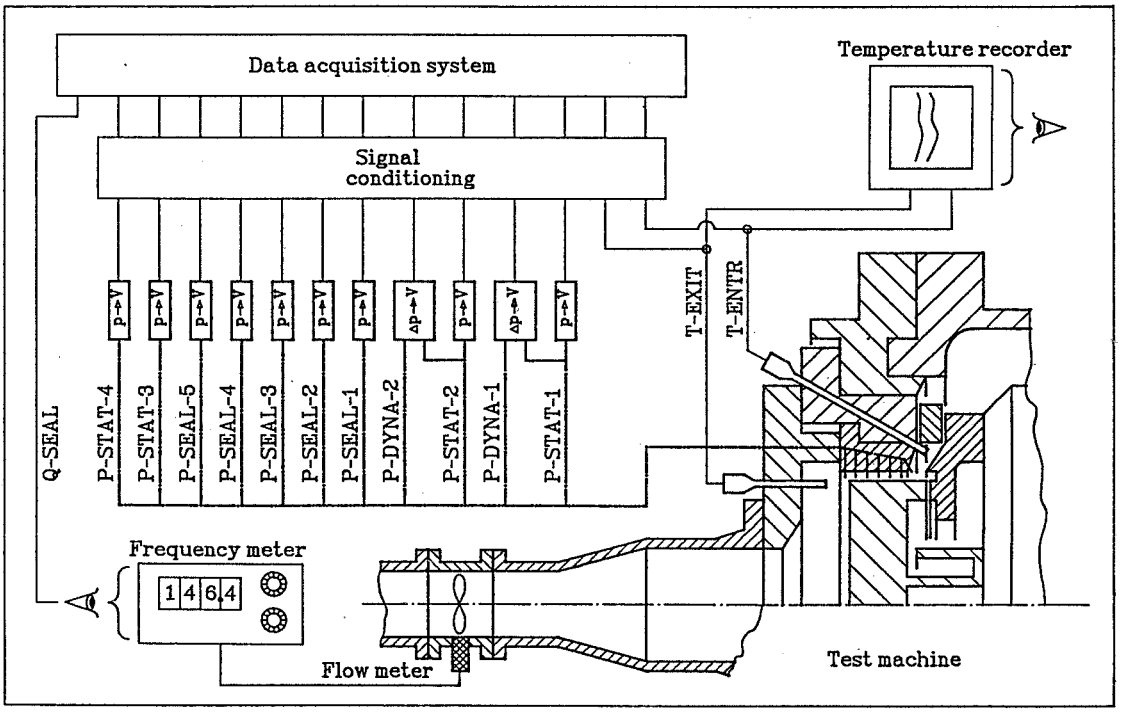

Figure 9. - Measurement of operating conditions.

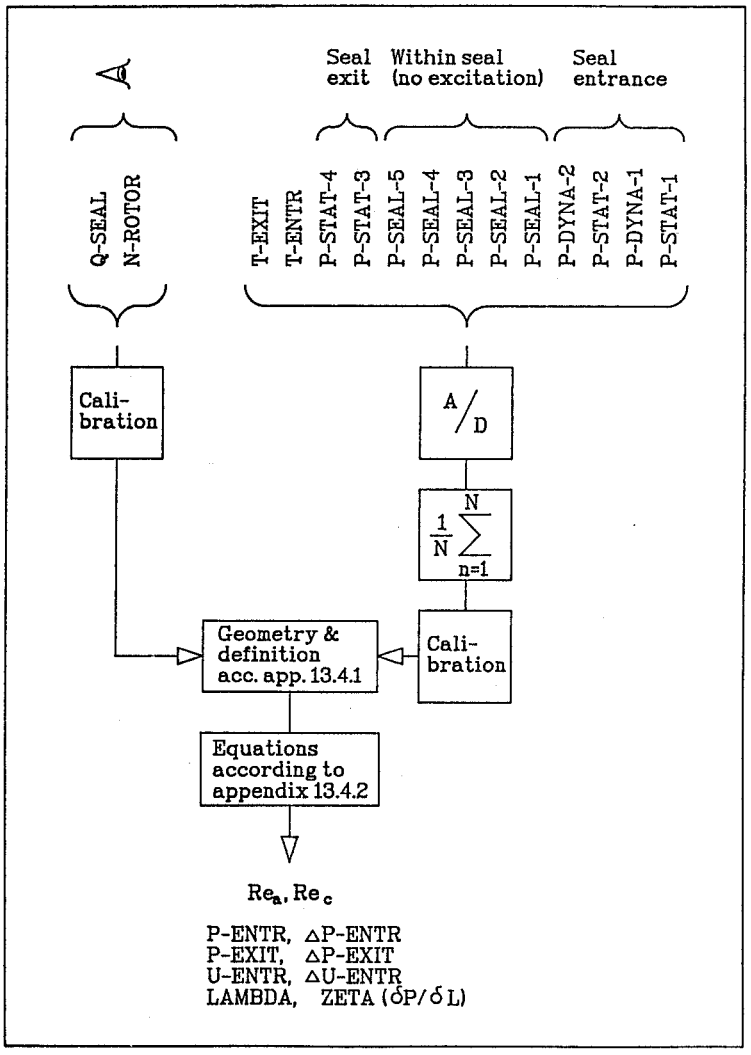

Figure 10. - Signal processing (operating conditions).

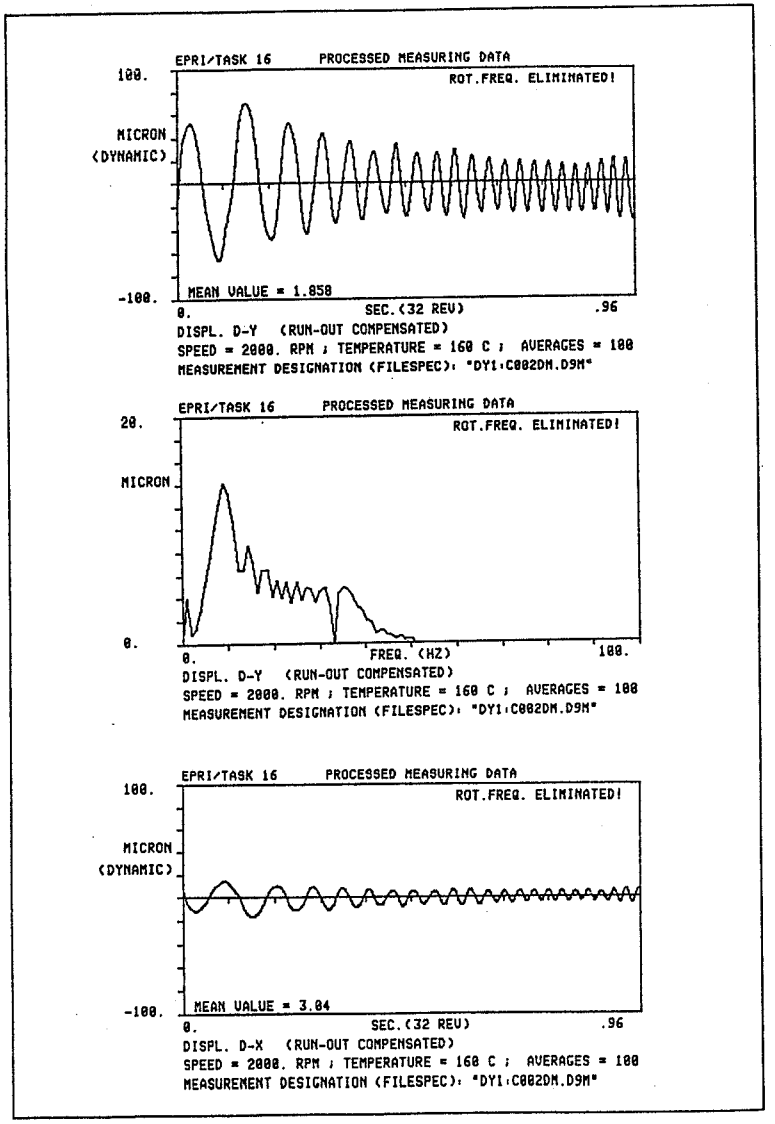

Figure 11. - Resulting displacement, serrated seal.

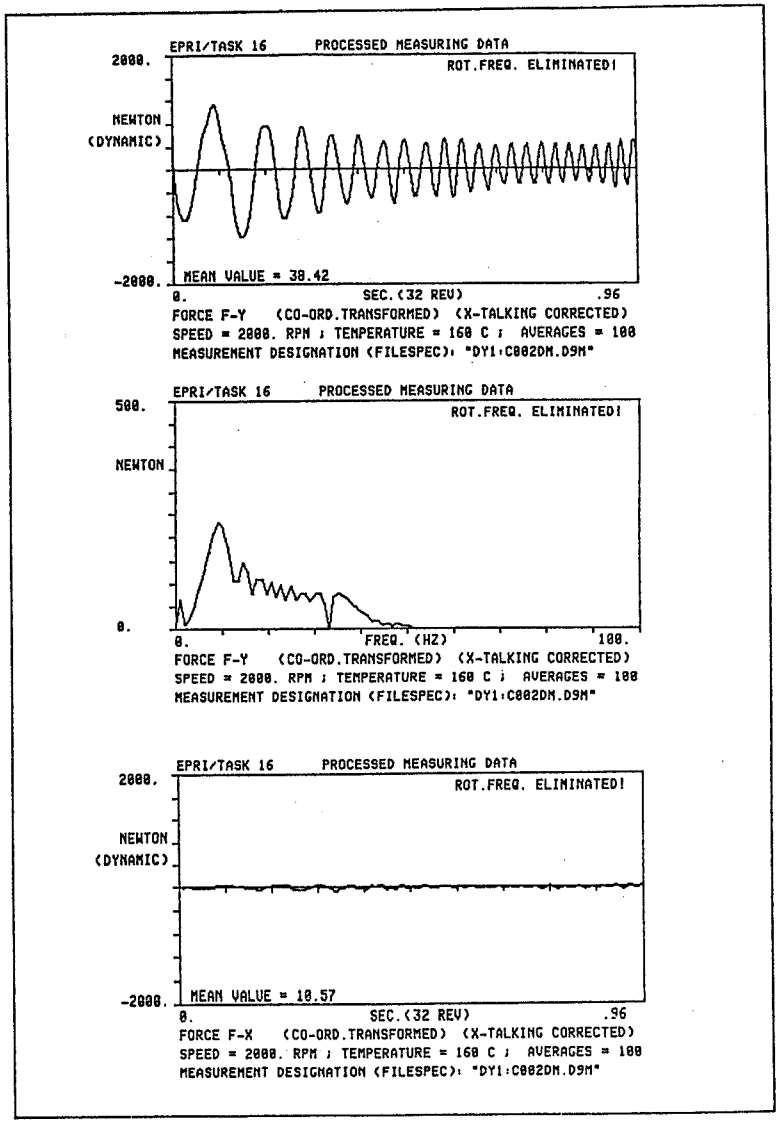

Figure 12. - Resulting forces, serrated seal.

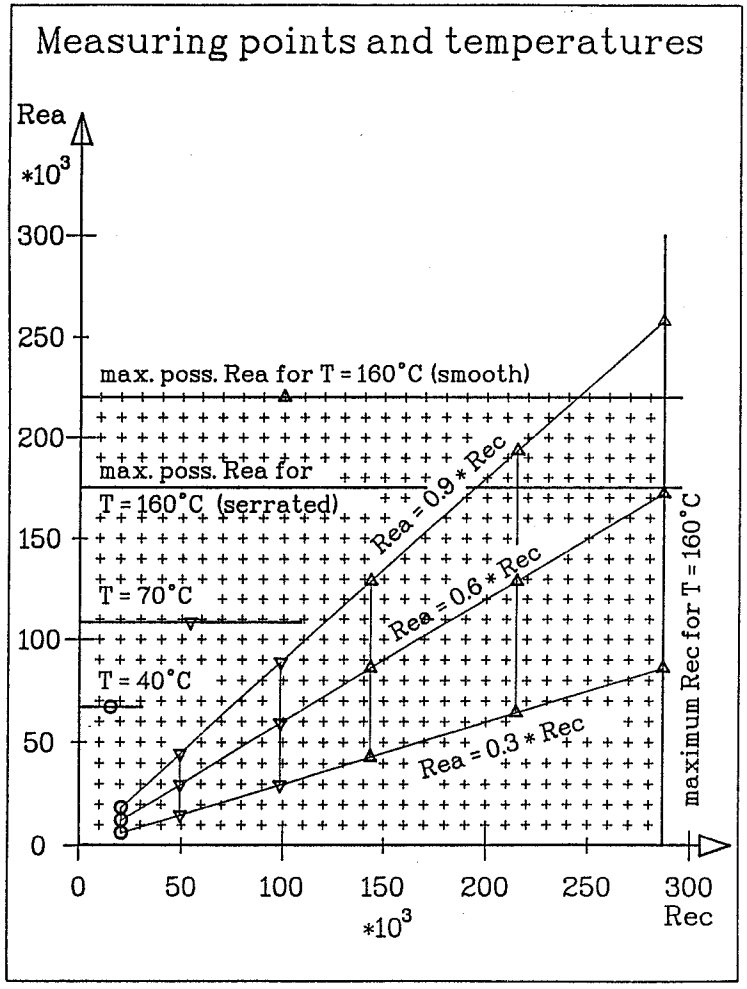

Figure 13. - Measuring range Re_c - Re_a.

Seal diameter:	350	mm	13.78	in
stepped:	350/325	mm	13.8/12.8	in
Radial clearance:	0.37	mm	0.015	in
double:	0.74	mm	0.03	in
Seal length:	40	mm	1.57	in
Water temperature:	20/70/80/160	°C	68/158/176/320	°F
Max. pump speed:	4000	rpm		
Max. pressure difference:	appr. 60	bar	870	p.s.i.
Max. circumf. Re-number:	275'000	[-]		
Max. axial Re-number:	175'000 (rough) 225'000 (smooth)			

TYPICAL VALUES FOR BFP'S:

Re_a / Re_c = 0.4 to 0.9 (measured 0,3 ; 0,6 & 0,9)

Re_c = 200'000 to 260'000

Re_a = 100'000 to 150'000

Figure 14. - Test parameters.

Geo-metry	Seal type	Surface	Gap width	Inlet swirl	Tempe-rature	Sketch
00S	straight	plain N8/N8	2.11 ‰	0.25 + Variation at 4 Points	40/70/160	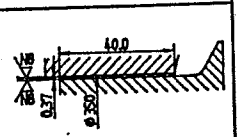
04S	straight	serrated N8/N8	2.11 ‰	0.15 + Variation at 4 Points	40/70/160	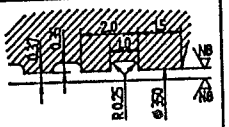
04D	straight	serrated N8/N8	4.23 ‰	0.15 + Variation at 4 Points	40/70/160	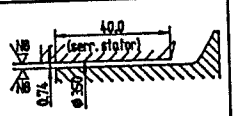

Definition of surface roughness acc. ISO 1302-1926

VSM 10231	Maximum allowable Surface roughness [1E-6 m]
N9	6,3
N8	3,2
N7	1,6
N6	0,8

Definition of near surface roughness value Ra

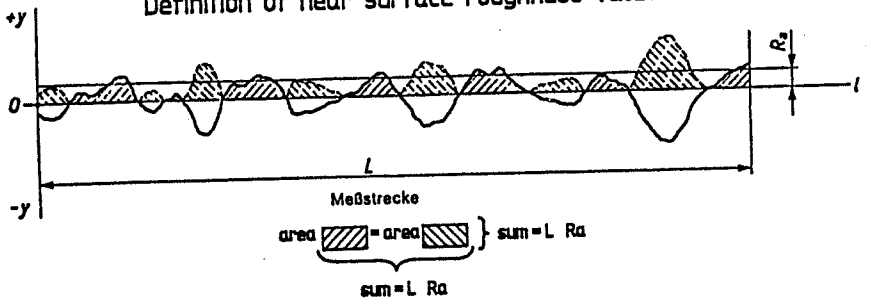

Figure 15. - Seal configurations.

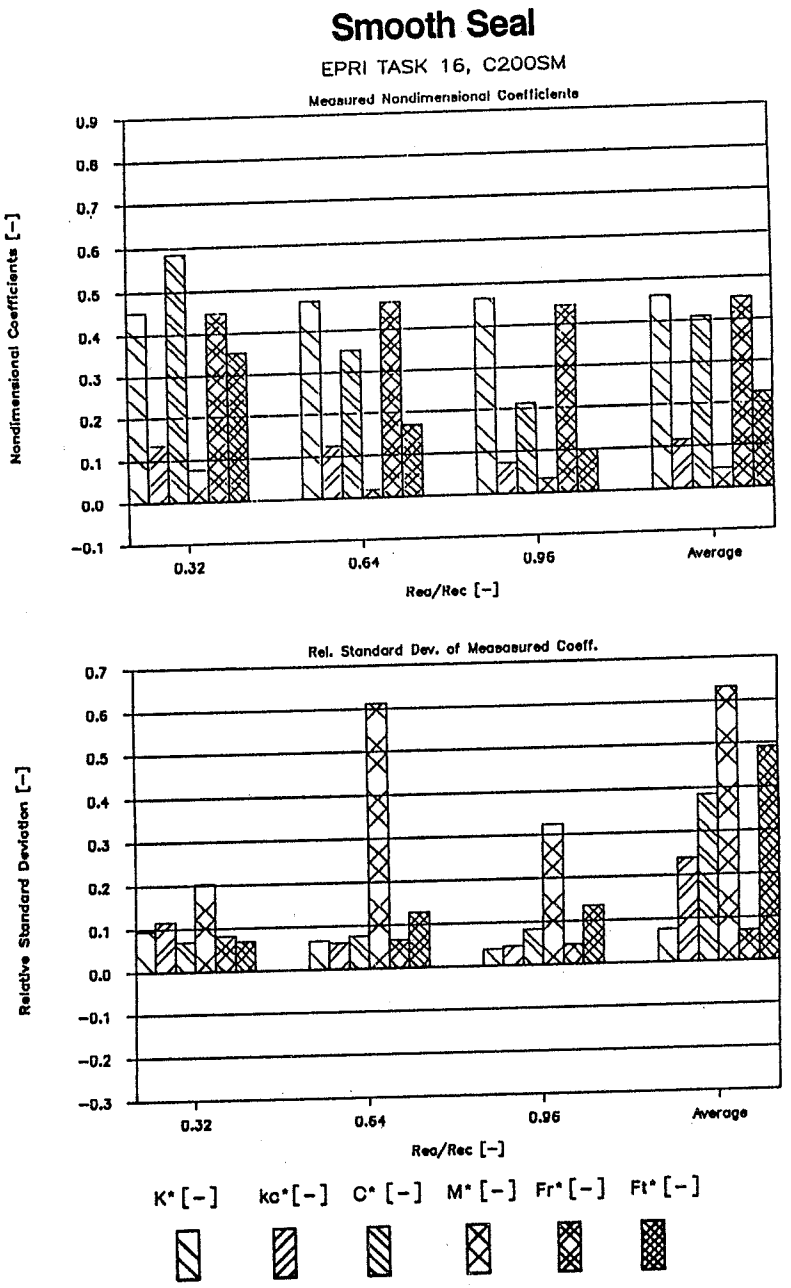

Figure 16. - Test 00S-M, averaged coefficients, f(Re-ratio).

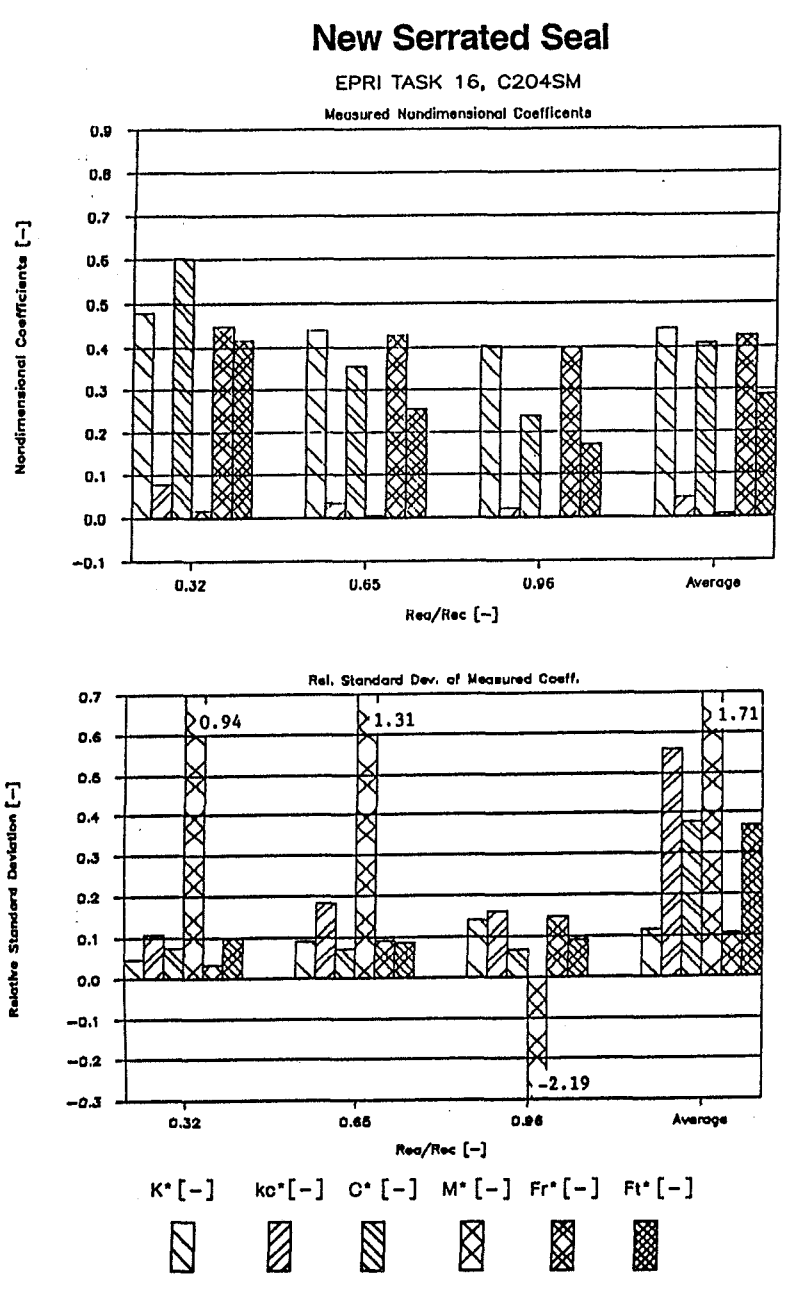

Figure 17. - Test 04S-M, averaged coefficients, f(Re-ratio).

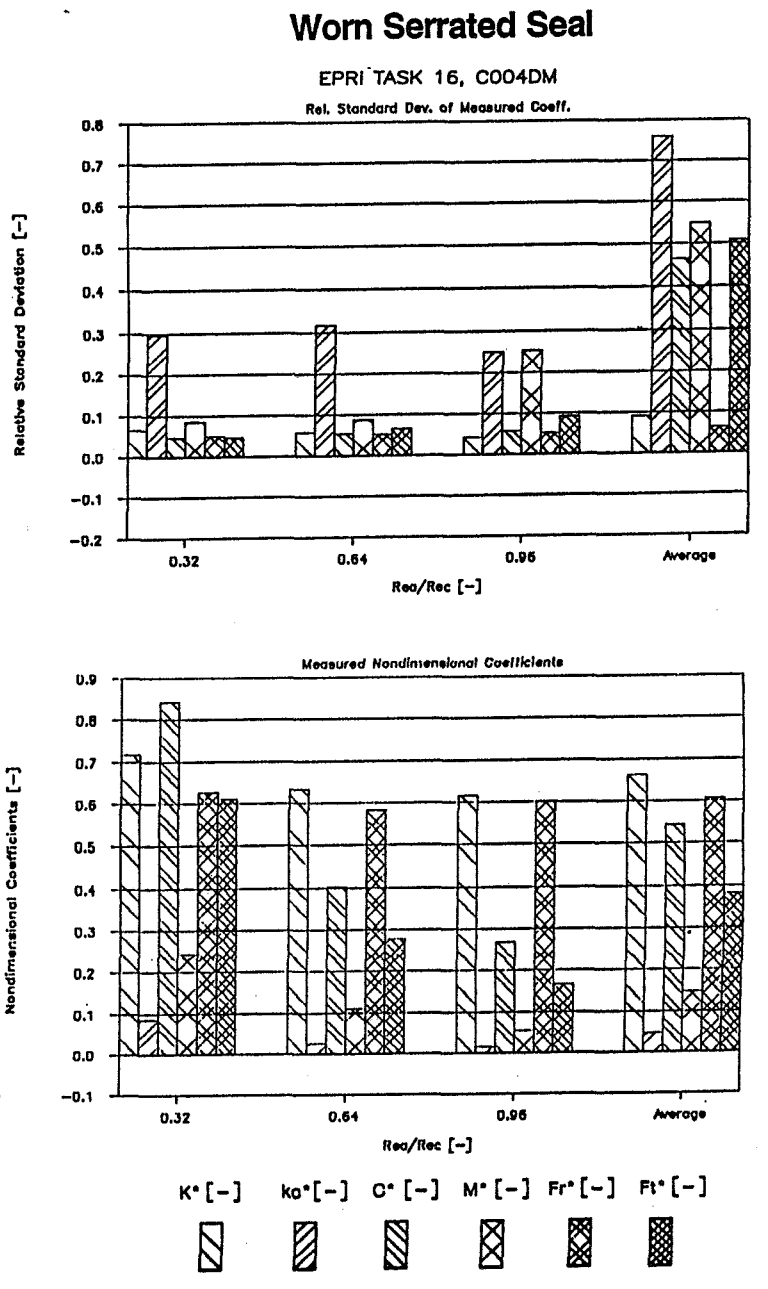

Figure 18. - Test 04D-M, averaged coefficients, f(Re-ratio).

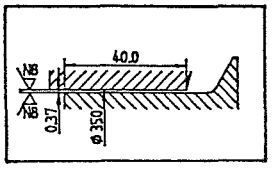

Re_a/Re_c:	Re_c/1E3:	Re_c/1E3:
0.63 0.96	⊙ 47.4 △ 47.6	+ 130.7 × 130.5

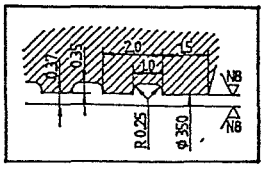

Re_a/Re_c:	Re_c/1E3:	Re_c/1E3:
0.63 0.95	⊙ 48.3 △ 48.0	+ 132.8 × 133.5

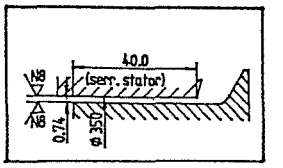

Re_a/Re_c:	Re_c/1E3:	Re_c/1E3:
0.62 0.93	⊙ 95.6 △ 95.6	+ 271.4 × 272.4

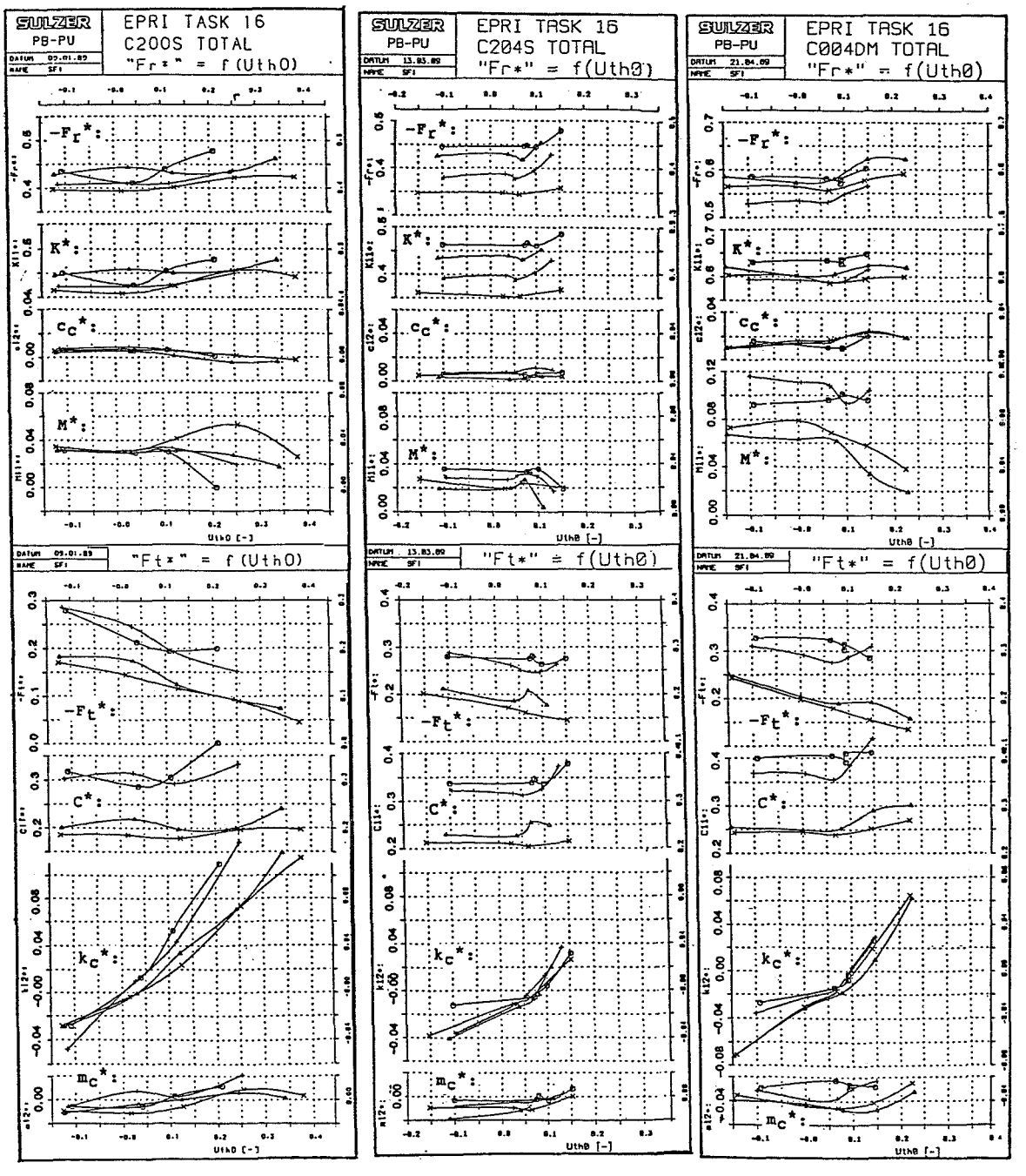

Figure 19. - All tests, coefficients = f(U_{th0}).

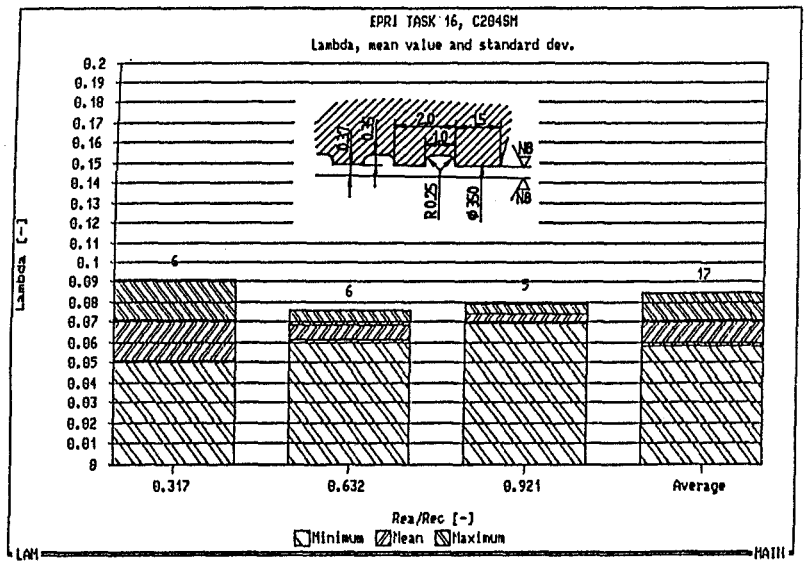

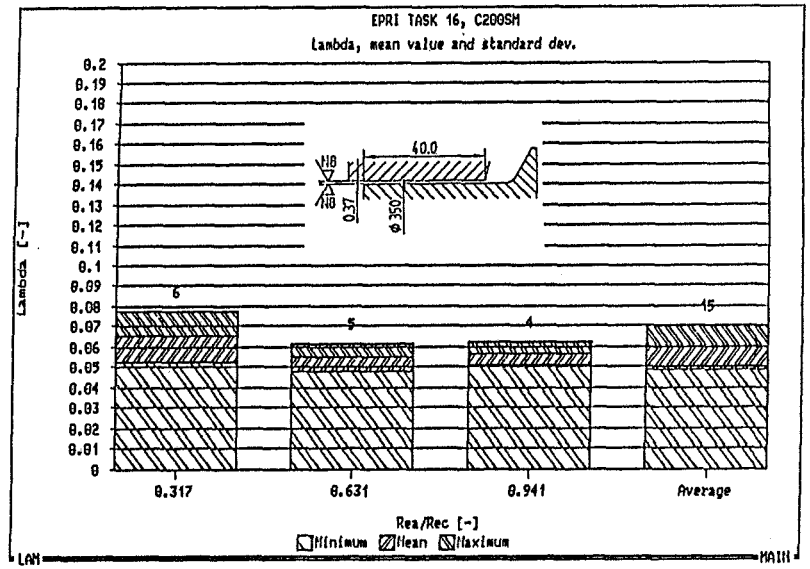

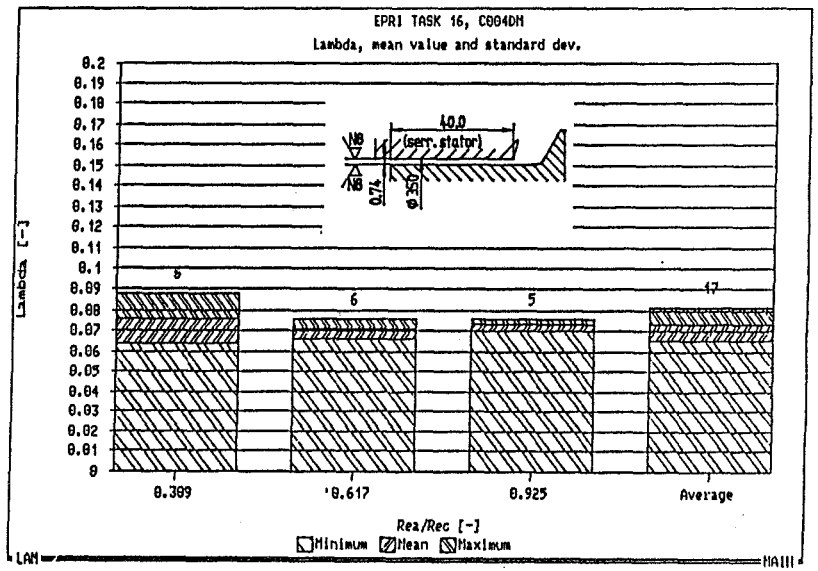

Figure 20. - Lambda bar charts for all tests.